The Astrophysical Journal, 798:85 (12pp), 2015 January 10 doi:10.1088/0004-637X/798/2/85

CO GAS INSIDE THE PROTOPLANETARY DISK CAVITY IN HD 142527: DISK STRUCTURE FROM ALMA

S. Perez[1,2], S. Casassus[1,2], F. Ménard[2,3,4], P. Roman[2,5], G. van der Plas[1,2], L. Cieza[2,6], C. Pinte[3,4], V. Christiaens[1,2], and A. S. Hales[2,7]
[1] Departamento de Astronomía, Universidad de Chile, Casilla 36-D, Santiago, Chile
[2] Millenium Nucleus "Protoplanetary Disks in ALMA Early Science," Universidad de Chile, Casilla 36-D, Santiago, Chile
[3] UMI-FCA 3386, CNRS/INSU, Casilla 36-D, Santiago, Chile
[4] Univ. Grenoble Alpes, IPAG, F-38000 Grenoble, France CNRS, IPAG, F-38000 Grenoble, France
[5] Center of Mathematical Modelling, Universidad de Chile, Chile
[6] Facultad de Ingeniería, Universidad Diego Portales, Av. Ejército 441, Santiago, Chile
[7] Joint ALMA Observatory, Alonso de Córdoba 3107, Vitacura 763-0355, Santiago, Chile
Received 2014 January 23; accepted 2014 October 27; published 2014 December 29

ABSTRACT

Inner cavities and annular gaps in circumstellar disks are possible signposts of giant planet formation. The young star HD 142527 hosts a massive protoplanetary disk with a large cavity that extends up to 140 AU from the central star, as seen in continuum images at infrared and millimeter wavelengths. Estimates of the survival of gas inside disk cavities are needed to discriminate between clearing scenarios. We present a spatially and spectrally resolved carbon monoxide isotopologue observations of the gas-rich disk HD 142527, in the $J = 2$–1 line of ^{12}CO, ^{13}CO, and C^{18}O obtained with the Atacama Large Millimeter/submillimeter Array (ALMA). We detect emission coming from inside the dust-depleted cavity in all three isotopologues. Based on our analysis of the gas in the dust cavity, the ^{12}CO emission is optically thick, while ^{13}CO and C^{18}O emissions are both optically thin. The total mass of residual gas inside the cavity is $\sim$1.5–2 $M_{\rm Jup}$. We model the gas with an axisymmetric disk model. Our best-fit model shows that the cavity radius is much smaller in CO than it is in millimeter continuum and scattered light observations, with a gas cavity that does not extend beyond 105 AU (at 3σ). The gap wall at its outer edge is diffuse and smooth in the gas distribution, while in dust continuum it is manifestly sharper. The inclination angle, as estimated from the high velocity channel maps, is 28 ± 0.5 deg, higher than in previous estimates, assuming a fix central star mass of 2.2 $M_{\odot}$.

Key words: protoplanetary disks – stars: individual (HD 142527)

1. INTRODUCTION

Planets are thought to form within circumstellar material, in so-called protoplanetary disks (e.g., Armitage 2010). As these planets grow massive, they imprint a series of morphological and dynamical features onto their parent disk. During their formation epoch, one or multiple massive planets could open a gap in a gas-rich protoplanetary disk (Varnière et al. 2006; Zhu et al. 2011). The surface density profile of the gap is determined by the balance between gravity, viscous and pressure torques (Crida et al. 2006). Evidence of these gaps has been observed at various wavelengths in nearby young stars (e.g., Andrews et al. 2011).

The star HD 142527, with spectral type F6IIIe, hosts a protoplanetary disk with a large infrared excess (Malfait et al. 1999; Fukagawa et al. 2006). It is a young gas-rich system, with an estimated age of $\sim$2 Myr (Fukagawa et al. 2006). HD 142527 is most likely embedded inside the Lu22 condensation of the Lupus dark cloud, at a distance of 140 pc away, which has a reported $V_{\rm LSR} = 4.69 \pm 0.7\,{\rm km\,s^{-1}}$ (Vilas-Boas et al. 2000). Its disk is almost face-on with an inclination of $\sim$20°, from previous infrared data. The disk exhibits a remarkably large dust-depleted cavity extending out to a radius of $\sim$140 AU, as seen in IR imaging (Fukagawa et al. 2006), submillimeter continuum and CO line emission (Ohashi 2008; Casassus et al. 2013b). The outer disk has a complex nonaxisymmetric surface density showing several spiral arms and clumps (Rameau et al. 2012; Avenhaus et al. 2014), signs of dynamical perturbation possibly caused by planetary-mass bodies inside the cavity or gravitational instability (Christiaens et al. 2014).

Recent ALMA observations of HD 142527 have evidenced what could be key stages of the planet formation process: the discovery of gaseous flows inside the dust-depleted cavity, as seen in HCO+ emission by Casassus et al. (2013b). Resolved CO $J = 3$–2 observations show a peak in emission in the cavity, in agreement with ongoing dynamical clearing by planetary-mass bodies (Bruderer 2013). Also using ALMA, Fukagawa et al. (2013) found that the $J = 3$–2 isotopologues, ^{13}CO and C^{18}O, are optically thick in the outer disk.

Detection of gas inside a protoplanetary gap provides quantitative information on the total gas mass content and temperature profile, depending on whether the line emission is optically thin or optically thick (Wilson et al. 2009). Direct images and estimates of the survival of the gas inside transition disk cavities are needed to discriminate between scenarios of dust removal, such as grain growth, photoevaporation, and planet–disk interactions. For instance, grain growth is not expected to markedly affect the gas density profile, while photoevaporation removes both dust and gas (Bruderer 2013). One way of discriminating between a planet-induced gap and a photoevaporation-induced gap can be based on the sharpness of the transition in surface density at the outer edge of the cavity: dynamical clearing would result in a rather sharp transition if the putative planet is massive (Pascucci et al. 2011). Millimeter observations of the rotational gas lines are ideal to quantify the amount of gas inside a dust-depleted cavity. Moreover, by comparing isotopologue emission from specific regions of the disk in protoplanetary systems we can constrain physical properties of the disk, such as its gas density and gas temperature.

Resolved observations of optically thin emission can directly trace the underlying mass density distribution in the disk cavity. The amount of gas inside a protoplanetary cavity can provide constrains on planet formation and migration scenarios. For example, a planet that is not massive enough to cleanly evacuate the material inside the gap will only decrease the disk surface density. Also, such planet is expected to co-orbit with a corotation zone, which should carry significant amounts of gas (Armitage 2011). Thus, studying the gas surface density structure of transition disks is of direct importance to distinguish between different clearing and formation scenarios.

In this paper, we analyze ALMA Band 6 (∼230 GHz) CO line emission and dust continuum observations of HD 142527. The data provide resolved observations of gas inside a dust depleted protoplanetary disk cavity. Our analysis aims to measure the amount of gas in this cavity and provide a more complete picture of the structure of the HD 142527 disk. The interferometric ALMA data reduction and calibration steps are described in Section 2. A detailed description of the CO emission maps, the morphology and kinematics of the observed gas, along with diagnostics of the physical conditions inside the cavity, are provided in Section 3. We develop a disk structure model consistent with HD 142527 observations to study the properties of the disk. This model and the radiative transfer calculations are presented in Section 4.1. Data and modeling are combined and interpreted in the context of gas depletion mechanisms in Section 5. Section 6 summarizes the main results of this investigation. A brief description of HD 142527's spectral energy distribution (SED), as computed for the model presented in Section 4.1, is presented in the Appendix.

2. ALMA DATA AND PROCESSING

The HD 142527 Band 6 observations were acquired on 2012 April 12 and June 15 using sixteen and twenty 12 m antennas, respectively. In both observing sessions the precipitable water vapor in the atmosphere was stable between 1.5 and 2.0 mm with clear sky conditions, resulting in median system temperatures ranging from 70 to 90 K. The ALMA correlator was configured in the Frequency Division Mode (FDM) to provide 125 MHz bandwidth in four different spectral windows at 0.2 km s^{-1} resolution per channel. Three spectral windows were positioned in order to target the ^{12}CO J = 2–1, ^{13}CO J = 2–1, and C^{18}O J = 2–1 isotopologues at 230.538, 220.399, and 219.560 GHz, respectively. In both sessions Titan was observed as flux calibrator, while the quasars 3C 279 and J1604−446 were observed for bandpass and phase calibration, respectively. Observations of the phase calibrator were alternated with the science target every 8 minutes to calibrate the time dependence variations of the complex gains. The total time spent on-source was 82 minutes. However, the concatenated data set shows spurious spectral line features. Therefore, in this work we only used the June observations which have higher signal-to-noise and better uv coverage than the April data.

All the line data were calibrated using the *Common Astronomy Software Applications* package (CASA[8]; McMullin et al. 2007) in a standard fashion, which included offline Water Vapor Radiometer (WVR) calibration, system temperature correction, as well as bandpass, phase, and amplitude calibrations. The fluxes derived for 3C279 in April and June were 15.9 and 17.5 Jy, respectively. For J1604−446, the flux values after bootstrapping to the observations of Titan were 0.56 and 0.6 Jy in April and June. By considering the scatter in the fluxes derived for the bandpass and phase calibrators in the different observing sessions, we estimate the absolute flux calibration to be accurate within ∼10%.

Imaging of the CO lines was performed using the CLEAN task in CASA (Högbom 1974). The data set provides baselines up to 402 m, which resulted in a synthetic beam size of $0\farcs85\times0\farcs64$ at P.A.= $-66\fdg5$. Continuum subtraction in the visibility domain was performed prior to imaging of the CO lines. After CLEANing the images, an rms noise level of 11 mJy per 0.2 km s^{-1} channel was reached. In this paper, we also make use of the 345 GHz continuum data described in Casassus et al. (2013b).

The central cavity is resolved in the isotopologues data, with approximately four beams covering the gap. An astrometric correction was applied to the data set in order to account for the star's proper motion of (−11.19, −24.46) mas yr^{-1}, as measured by *Hipparcos* (van Leeuwen 2007). This implied a shift in the images of 0.3 arcseconds since epoch J2000.

3. RESULTS

3.1. Morphology and Kinematics of the Gas Disk

Molecular gas observations, such as millimeter/submillimeter pure rotational lines of CO, can provide constraints on the amount of gas mass inside transition dust-depleted disk cavities. The dust-depleted cavity in HD 142527 has an apparent size of ∼2″ across (Casassus et al. 2012). Our ALMA Cycle 0 observations have enough sensitivity and resolution to detect and resolve such leftover gas in HD 142527 cavity.

3.1.1. Moment Maps

Figure 1 shows the integrated intensity, velocity centroid, and velocity dispersion for the three isotopologues. All the moment maps velocity information displayed in Figure 1 were derived by fitting a Gaussian profile to the spectral axis in each spatial pixel of the CLEANed data cubes. The maps were then median-filtered with a kernel box of $0.1\times0\farcs1$. We detect extended ^{12}CO emission, 5σ above the noise level, as far as 5″ away from the center, which corresponds to ∼700 AU (see Christiaens et al. 2014, for a discussion of the extended features seen in ^{12}CO).

The ^{12}COJ = 2–1 integrated emission (Figure 1, or zeroth-order moment map $I(^{12}\mathrm{CO})$ (Figure 1, upper left) is smooth, with no counterpart of the cavity seen in the CO isotopologues. In fact, $I(^{12}\mathrm{CO})$ peaks inside the dust-depleted cavity, at a location close to the star but intriguingly shifted to the north by $0\farcs4$ (about half a beam). The stellar position, as tabulated in the SIMBAD database, is consistent with the disk's expected center as given by the center of symmetry in the velocity field (represented with a black cross in Figure 1). The lack of a decrement in $I(^{12}\mathrm{CO})$ outlining the cavity, as seen in its rarer isotopologues, suggests that the line is most likely optically thick (see Section 3.3).

The asymmetric morphology of the emission and its off-centered peak are due to absorption by an intervening cloud, at 4.4 km s^{-1} (Casassus et al. 2013a), thus affecting the red part of the line. The foreground cloud can be seen as an absorption feature in the ^{12}CO spectrum shown in Figure 2. We measure the systemic velocity at 3.6 ± 0.1 km s^{-1} from the integrated CO spectra, by assuming that the line wings are symmetric (see Figure 2). The error is given by half the size of a spectral bin.

The HD 142527 dust continuum at 230 GHz, shown as contours in Figure 1, has a horseshoe-shaped morphology,

[8] http://casa.nrao.edu/

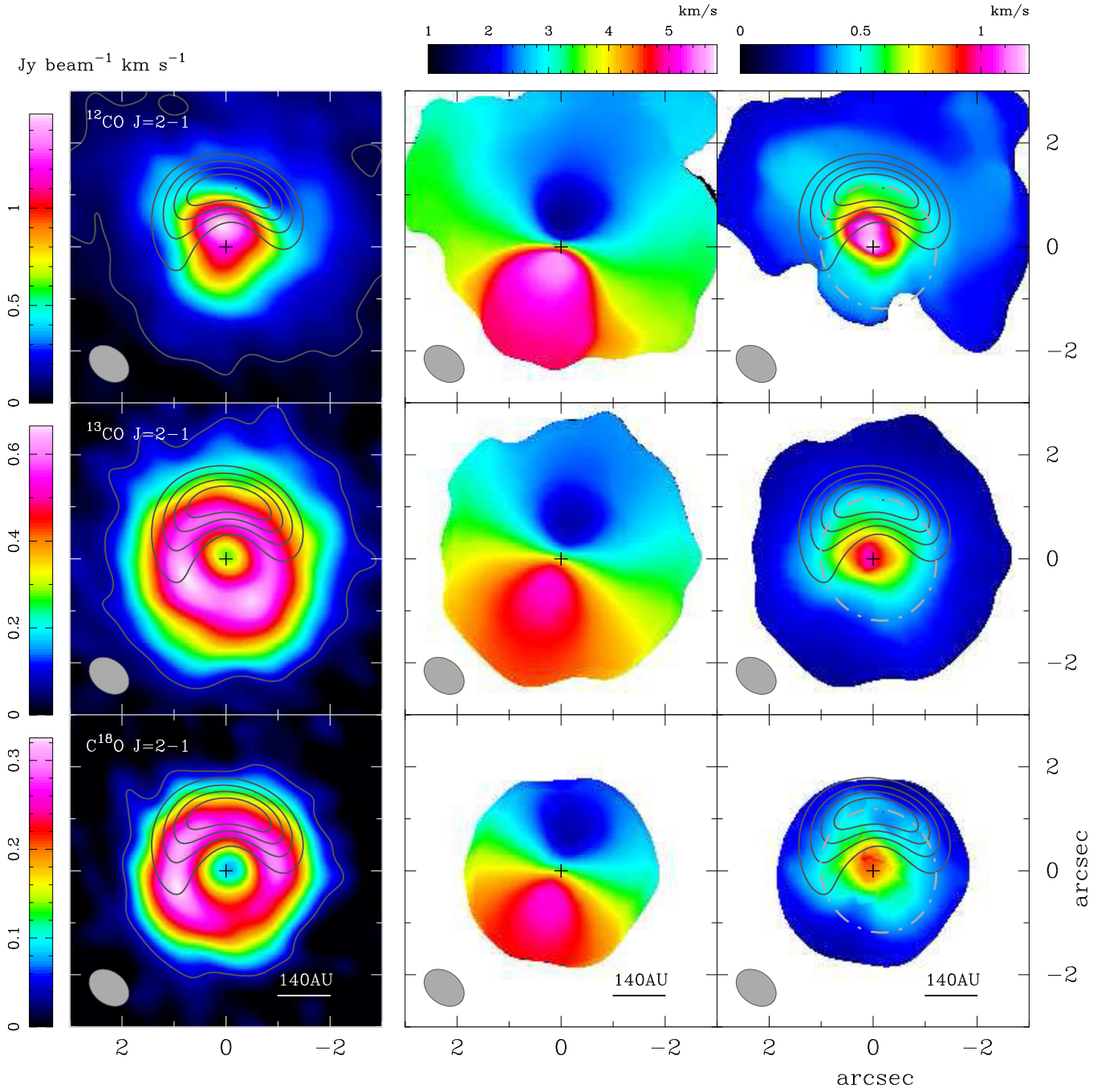

Figure 1. Moment maps carbon monoxide isotopologues ^{12}CO, ^{13}CO and C^{18}O$J = 2$–1. North is up, east is left. Left: moment zero; continuum subtracted integrated line emission, considering flux contribution from all channels from −0.8 to +7.8 km s^{-1}, in units of Jy beam^{-1} km s^{-1}. Continuum at 230 GHz is shown in contours. The ^{12}CO map shows the large extent of the molecular line emission, the north–south asymmetry is due to foreground absorption. ^{13}CO and C^{18}O show a central cavity. The noise level for all intensity maps is about $1\sigma = 11$ mJy per beam. Center: first moment showing the velocity map. Right: second moment, showing the velocity dispersion of the emitting gas. Color scale is linear. The coordinates origin is set to the center of the disk and it is marked with a cross. The synthesized beam is shown in the lower left corner. The dashed ellipse in the moment 2 map is a fit by inspection of the dust-continuum horseshoe border. The ellipse shows that there is a difference in dispersion of the gas under the horseshoe, with respect to the south counterpart of the disk.

as previously reported in Casassus et al. (2013b) at 345 GHz. The contours delineate the dust-depleted cavity, with a radius of ∼1″ and a contrast of ∼25 between the northeastern maximum and the southwestern minimum, slightly shallower than the contrast of 30 reported at 345 GHz (Casassus et al. 2013b; Fukagawa et al. 2013). The ^{13}CO integrated intensity map (Figure 1) shows a disk cavity and a bright outer disk. The outer disk is at least a factor of two brighter than the inner cavity in ^{13}CO. This is a lower limit since the gap edge is naturally convoluted with the CLEAN beam, smoothing out the sharpness of the gap wall.

The velocity dispersion map of ^{12}CO shows an increment in the width of the emission line profile under the horseshoe-shaped continuum (see dashed ellipse in Figure 1 upper right). This wider emission line can also be seen in the ^{13}CO dispersion map (middle right panel), which is less affected by foreground absorption.

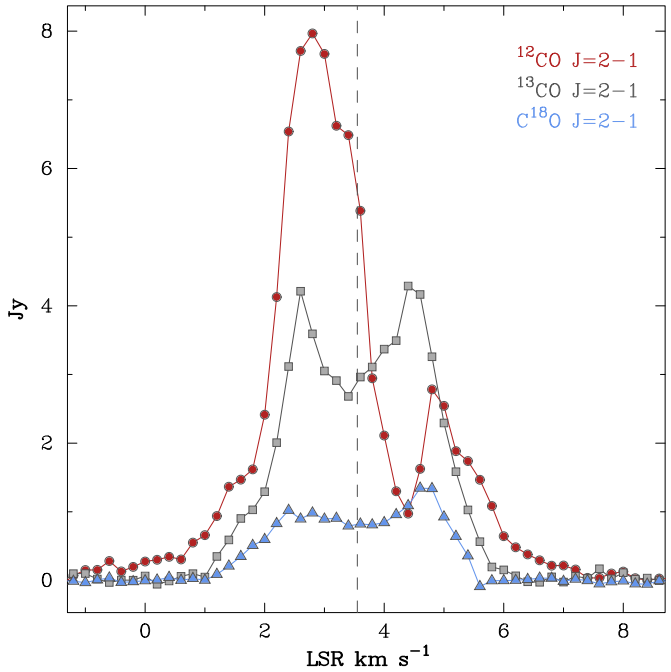

Figure 2. Continuum-subtracted ^{12}CO (circles), ^{13}CO (squares), and C^{18}O (triangles) $J = 2$–1 emission line spectra. The spectra are extracted summing over the whole data cube. Vertical dotted line corresponds to systemic velocity of 3.6 km s^{-1}, as determined from the ^{12}CO channel maps.

Table 1
Properties of Emission Line and Continuum Maps

Line ($J = 2$–1)	ν (GHz)	Beam ($''$)	1σ Noise (Jy beam^{-1})	Peak I_ν (Jy beam^{-1})	Flux[a] (Jy)
^{12}CO	230.538	0.85 × 0.64	0.012	0.74	17.4
^{13}CO	220.399	0.85 × 0.64	0.013	0.70	11.4
C^{18}O	219.560	0.85 × 0.64	0.013	0.39	3.4
Continuum					
Cont.	225.393	0.94 × 0.72	0.0003	0.27	1.09

Notes. Line emission and continuum maps properties. Maps were cleaned with CASA and binned to $\Delta v = 0.20$ km s^{-1} spectral resolution.

[a] Total flux integrated over the whole data cube ($\sim 10'' \times 10''$ aperture).

3.1.2. Channel Maps

Figures 3–5, show channel maps for ^{12}CO, ^{13}CO and C^{18}O emission from HD 142527. The Keplerian disk can be identified in the channel maps as butterfly-shaped emission. Properties of the maps, rms noise estimates, and peak and integrated line intensities for each isotopologue are listed on Table 1. Data were binned to 0.2 km s^{-1} per channel in LSR velocity. Maps were reconstructed with CLEAN using Briggs weighting. The CO lines were detected at 3σ level over a broad velocity range. ^{12}CO was detected from −0.8 to +7.8 km s^{-1} in LSR. ^{13}CO was detected between +1.0 and +6.2 km s^{-1}, while C^{18}O between +1.0 and +5.4 km s^{-1}.

An emission line originating from a disk in Keplerian rotation is expected to show a dipole field pattern on the surface of the disk, when binned in velocity (Horne & Marsh 1986). The low velocity channels, close to systemic velocity ∼3.6 km s^{-1}, have a Keplerian rotation profile, along a NE to SW position angle. Gas emission coming from inside the 140 AU dust-depleted cavity can be identified in the high velocity channel maps. Assuming a Keplerian velocity profile and the system parameters listed in Table 2, the observed emission from channels at velocities <+1.8 km s^{-1} and >+5.4 km s^{-1} is radiated by gas material contained in a radius of 140 AU (∼1$''$), thus coming entirely from inside the dust-depleted cavity.

Table 2
Parameters of Gas Disk Structure

Parameter	Units	Value	1σ error
i	deg	28	0.5[a]
$R_{\rm cav}$	AU	90	5
$\delta_{\rm gap}$		0.02	
$M_{\rm cav}$	$M_\odot$	2×10^{-3}	1×10^{-3}
$\log \Sigma_c$	m^{-2}	28.69	···
$M_\star$	$M_\odot$	2.2	···
h/r	···	0.1	···
γ	···	1	···
R_c	AU	200	···
$V_{\rm sys}$	km s^{-1}	3.6	0.1

Notes. We report 1σ error bars. Only parameters that have been optimized bear uncertainties.

[a] Assuming a fixed star mass of 2.2 $M_\odot$.

We note that gas emission coming from very near the central star shows signatures of non-Keplerian kinematics. This is evidenced by a change in position angle of the emission in the high velocity channels. For instance, the +0.0 km s^{-1} channel map has a P.A. that is shifted toward the NE, when comparing to the systemic velocity P.A. (near channel +3.6 km s^{-1}). Moreover, the red counterpart of that high velocity channel, the +7.2 km s^{-1}channel, has a P.A. shifted in the opposite direction, toward SW. If the gas inside the cavity is indeed being accreted onto the star, the infalling material would have a radial velocity component that may explain the non-Keplerian emission at high velocity channels (Rosenfeld et al. 2014).

Another evident feature of the gaseous disk in HD 142527 can be seen in the ^{13}CO and C^{18}O channel maps. There is a decrement, meaning lower emission at a certain blue velocity channel when compared to its red counterpart, toward the NE of the disk. Compare, for example, channel +2.4 with +4.8 km s^{-1} in both isotopologues, where the red channel is a factor of nearly two brighter than the blue (also seen as a slight asymmetry in the integrated line profiles in Figure 2). This decrement is, to a moderate extent, coincident with the horseshoe-shaped continuum. Furthermore, van der Plas et al. (2014) presented HD 142527 imaging of the HCN $J = 4$–3 and CS $J = 7$–6 emission lines and showed that these lines are also suppressed under the horseshoe-shaped continuum emission peak.

3.2. A Cut Through the Inner and Outer Disks

Figure 6 shows a cut through the disk (near the major axis, at 2 hr) in integrated intensity. The profiles correspond to dust continuum at 345 and 230 GHz (black solid and dashed red lines, respectively) and ^{13}CO and C^{18}O isotopologues emission. All the profiles are double-peaked, with the peaks asymmetrical with respect to the center of the disk. The center of the disk is assumed to be the mid-point in between the two 345 GHz peaks. The dust emission is 40% weaker in the SE (left peak) than the NW (right peak), in opposition to the line emission which appears 10%–15% stronger in the SE. The ^{12}CO profile peaks inside the cavity, but it is heavily affected by foreground absorption, hence it is not included in Figure 6.

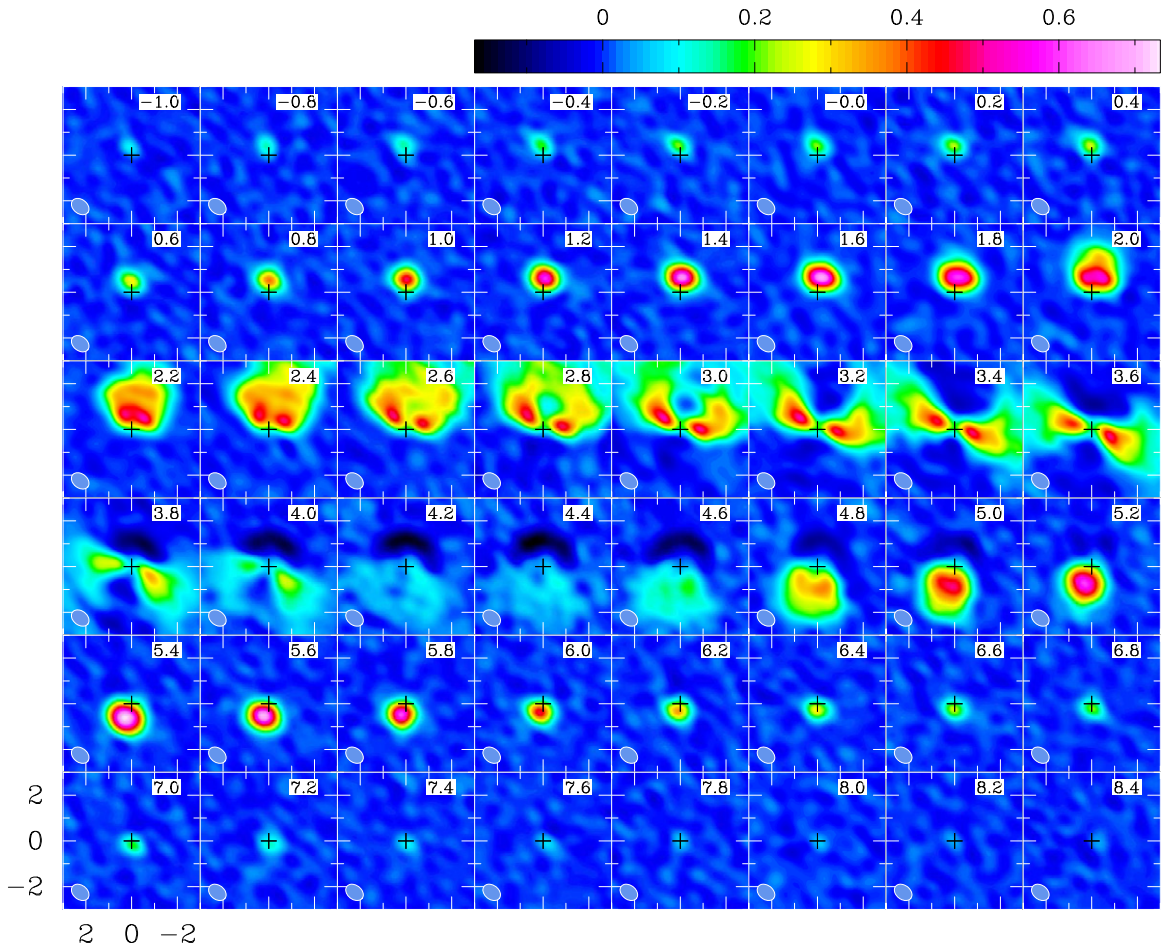

Figure 3. ^{12}CO $J = 2$–1 channel maps from CLEAN reconstruction in an exponential color scale. The LSR velocity for each channel is indicated in the upper right-hand corner in km s^{-1}. North is up, east is to the left. The systemic velocity of HD 142527 is 3.6 km s^{-1}. The synthesized beam is shown in the lower left-hand corner. The cross at origin represents the stellar position which most likely represents the center of rotation of the disk velocity profile. The color wedge is in units of Jy beam^{-1} km s^{-1}. The position of the disk center, which we assume is given by the center of symmetry of the emission at systemic velocity (channel at +3.6 km s^{-1}), is consistent with the estimated astrometry after correcting by the source's proper motion (black cross).

The 345 GHz (870 μm) continuum cut shows an unresolved compact emission near the center of the cavity. The centroid of this emission is shifted from the apparent center of the outer disk as given by the mid-point between the bright outer disk peaks (see vertical dot-dashed line in Figure 6). The mid-point between the peaks also coincides with the center of rotation of the CO gas. The shift is ∼0.″1 to the east and corresponds to a deprojected distance of ∼16 AU at 140 pc.

We roughly quantify the position and roundness of the disk wall in the continuum and in line emission by fitting a simple Gaussian function to each profile. The FWHM of the 230 GHz continuum peaks is both about 0.″9, so just resolved by our beam (the cut through the disk is along the beam's semi-minor axis), with peak centroids at −1.″07 and 1″. The 345 GHz continuum (band 7) peak widths are 0.″57 and 0.″53, for the west and east peaks, respectively.

The double-peaked morphology in ^{13}CO and C^{18}O in Figure 6 reveals a smaller and shallower gaseous cavity than the dust-depleted cavity traced by the continuum. Interestingly, the line emission presents a more complex profile than the continuum which we accounted for by fitting a Gaussian on top of a variable order polynomial function. The FWHM of the peaks in ^{13}CO are ∼1.″2 centered at −0.″75 and 0.″9 away from the disk origin, while C^{18}O is slightly narrower with FWHM of ∼1.″1 centered at −0.″9 and 1″, closer to the disk center. The CLEANed beam for the CO isotopologues (shaded region shown in Figure 6) is only 0.″6 across the cut axis, suggesting that the gap profile is indeed resolved by our gas observations. Therefore, the gas outer disk inner wall lies closer to the star, at 90 AU. The CO flux density appears more tapered toward the center than the millimeter dust. And, the outer disk inner wall is significantly broader in gas, 1.″2 in ^{13}CO, than in millimeter continuum, 0.″9 at 230 GHz.

3.3. Optical Thickness of the Lines

We can estimate the optical depths (τ_ν) of each isotopologue from their observed isotopic line ratio (e.g., Lyo et al. 2011). For this, we assume CO gas is distributed as an isothermal slab that is larger than the telescope beam. In this case, the isotopic line ratio R can be written as

$$R = \frac{T_{\rm B}(\nu_1)}{T_{\rm B}(\nu_2)} = \left(\frac{\nu_1}{\nu_2}\right)\frac{1-e^{-\tau_1}}{1-e^{-\tau_2}}, \quad (1)$$

where subindices "1" and "2" refer to two of the isotopologues, either ^{12}CO and ^{13}CO, or ^{13}CO and C^{18}O, respectively. We also

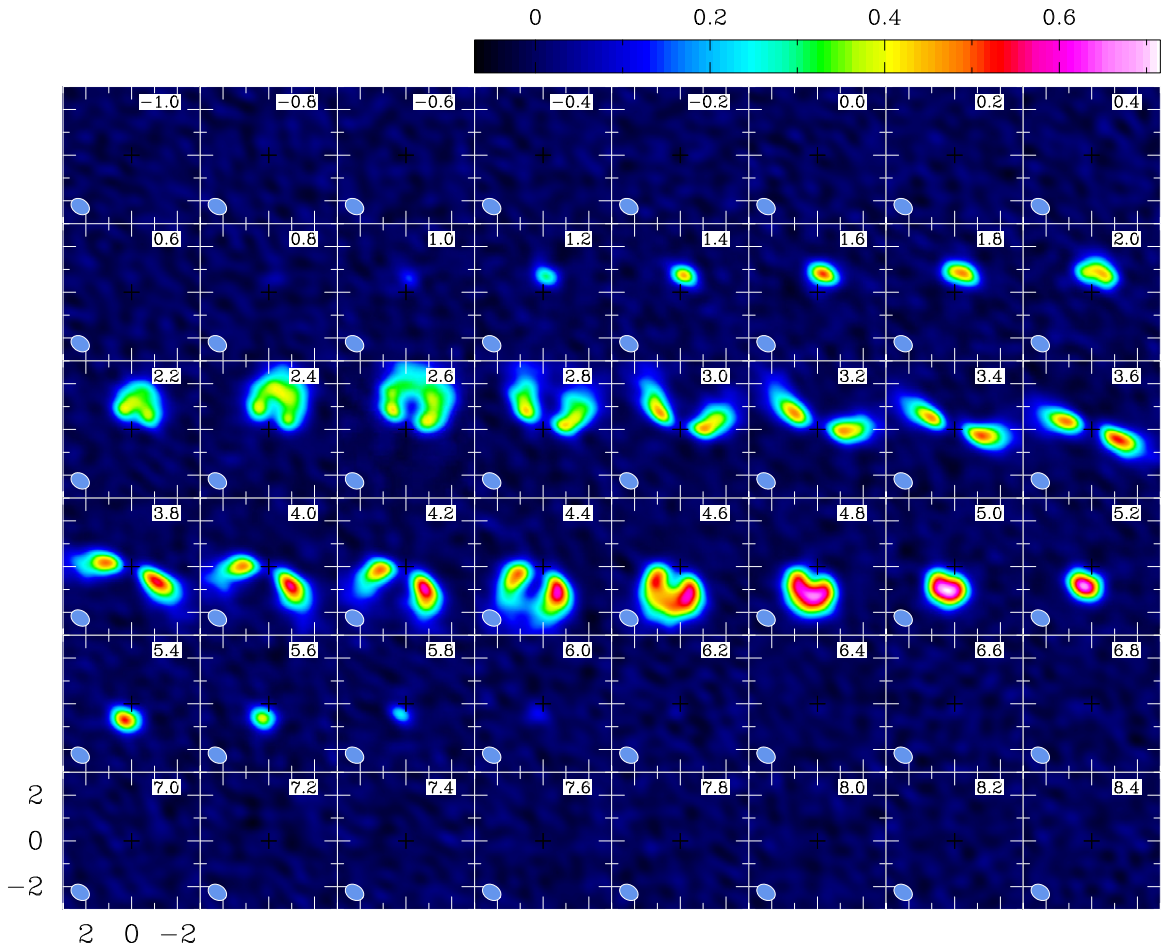

Figure 4. ^{13}CO channel maps in exponential color scale. For details, see caption in Figure 3.

assume that the two selected lines share the same excitation temperature, and that this temperature is high enough to neglect the contribution from the microwave background radiation. In this work, we adopt the ^{12}CO to ^{13}CO ratio of 76.27 ± 1.94 as measured in the ISM by Stahl et al. (2008; see also Casassus et al. 2005). The ^{12}CO to C^{18}O ratio is assumed to be the canonical value of 500 for the ISM (Wilson & Rood 1994).

The emission from channels at high rotational velocities, specifically at velocities $<+1.8\,\mathrm{km\,s^{-1}}$ and $>+5.4\,\mathrm{km\,s^{-1}}$, correspond to gas emitted solely from inside the dust cavity. From these channels, we can estimate the line ratios for the residual gas. In this velocity range, the isotopic line ratio R has a value of 2.0 ± 0.2, which yields optical depths of $\tau_{12\mathrm{CO}} \sim 56$ and $\tau_{13\mathrm{CO}} \sim 0.7$. Therefore, we conclude that inside the disk cavity ^{12}CO is optically thick, while ^{13}CO is mostly optically thin.

3.3.1. Temperature Profile from ^{12}CO

The observed ^{12}CO line is optically thick, hence the observed intensity map of the line traces the gas surface temperature rather than the underlying density distribution. The temperature profile for ^{12}CO seems to be nearly flat, $T(r) \sim$ constant, well inside the cavity (as measured from the emission in the high velocity channels), while it decreases with radius as $r^{-0.3}$ over the disk inner wall and outer disk, as estimated from the channel map at systemic velocity. The peak flux density of ∼1 Jy implies a gas temperature of 43 K for the ^{12}CO gas surface, measured at a radius of 80 AU.

3.4. Gas Mass Inside the Gap from ^{13}CO

The observed ^{13}CO line is optically thin inside the disk cavity, hence it gives an estimate of the gas mass content. The integrated line intensity of ^{13}CO emission, $\hat{I} = \sum_v I(v)\Delta v$, where $I(v)$ is the specific intensity measured at a channel with velocity v, and it is directly proportional to the total column density of the ^{13}CO gas. The channel width is $\Delta v = 0.2\,\mathrm{km\,s^{-1}}$. Assuming the CO gas is near LTE, the column density at the lower level $J = 1$ of the ^{13}CO molecule can be expressed by

$$N(1) = \frac{4\pi\,\hat{I}}{h\nu A_{21}}, \tag{2}$$

where $N(1)$ is the column density in level 1 expressed in $\mathrm{m^{-2}}$ units, A_{21} is the line strength given by the Einstein coefficient for spontaneous emission. The units for ν are Hz. Assuming that all energy levels are populated under LTE, the total population is given by the measured column density for a particular state J (in our case $J = 1$),

$$N(\mathrm{total}) = N(J)\frac{Z}{2J+1}\exp\left[\frac{hB_eJ(J+1)}{kT}\right], \tag{3}$$

where $Z = \sum_{J=0}^{\infty}(2J+1)\exp(-hB_eJ(J+1)/kT)$ is the Partition function. Here, B_e is the rotation constant.

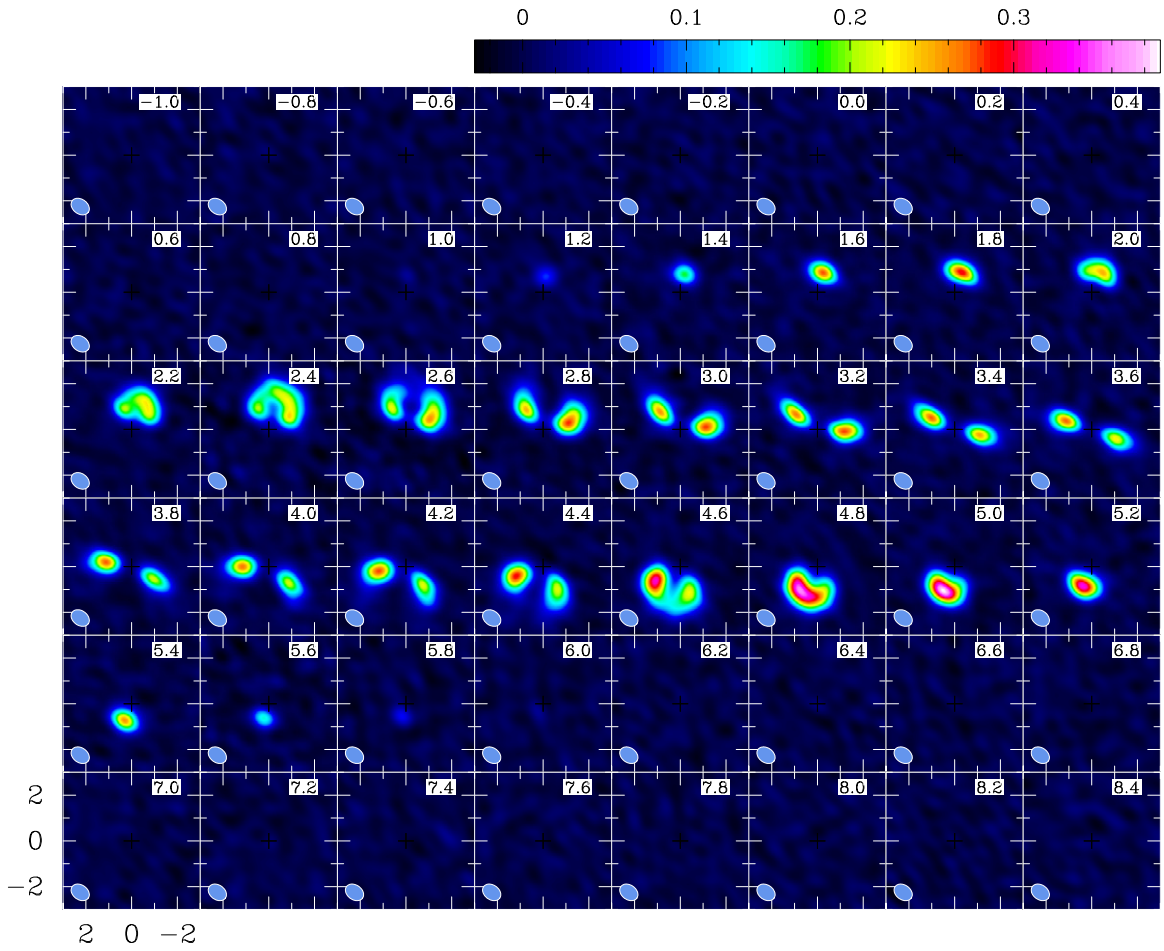

Figure 5. $C^{18}O$ channel maps in linear color scale. For details, see caption in Figure 3.

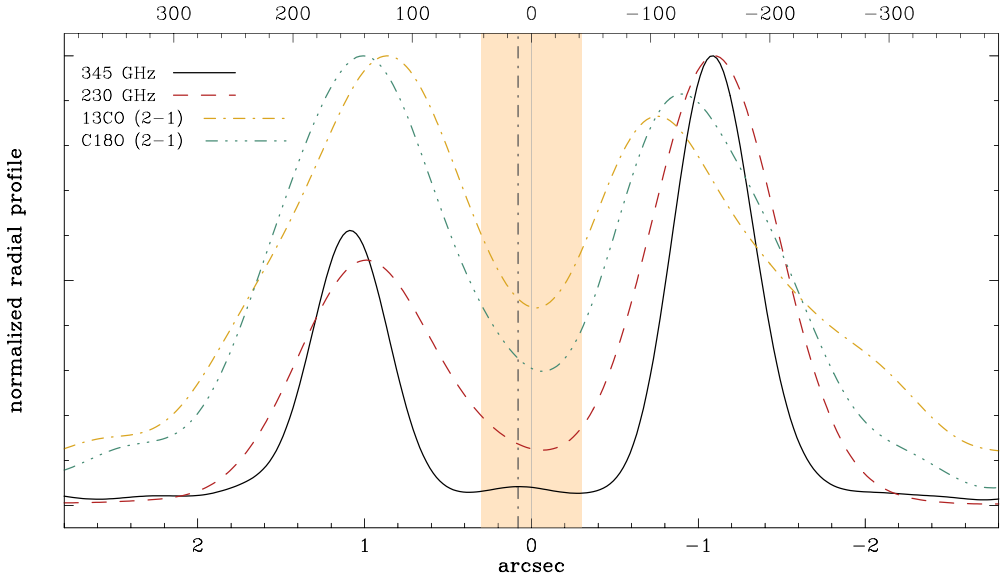

Figure 6. HD 142527 disk profile cuts extracted from the zeroth order moment maps (at 2h). Solid black and dashed red lines show integrated intensity of 345 GH and 230 GHz continuum, respectively. ^{13}CO and $C^{18}O$ $J = 2$–1 emission integrated intensity cuts are shown in yellow dot-dashed and green dot-dot-dashed lines. The shaded region shows the size of the beam across the cut axis. The extracted cuts have been scaled to the 345 GHz continuum peak to aid comparison between gas emission and dust. The bottom and top x-axes are in arcsec and AU, respectively. The beam size at 345 GHz is $0\farcs51 \times 0\farcs33$. The x-axis origin (solid vertical line) is given by the mid-point in between the two 345 GHz peaks, determined by fitting single Gaussians. The vertical dot-dashed line indicates the centroid of the faint central emission in 345 GHz continuum (see Section 3.2).

Assuming a fiducial CO interstellar abundance of $[H_2]/[^{12}CO] = 10^4$ and $[^{12}CO]/[^{13}CO] = 76$, the disk gas mass inside the dust cavity as estimated from ^{13}CO is given by

$$M_{\rm gas} = N({\rm total}) \left[\frac{^{12}{\rm CO}}{^{13}{\rm CO}}\right] \left[\frac{{\rm H_2}}{^{12}{\rm CO}}\right] \mu m_{\rm H_2} \Omega\, {\rm d}^2, \quad (4)$$

where $m_{\rm H_2}$ is the molecular mass of hydrogen, $\mu = 1.36$, Ω is the solid angle subtended by the cavity in ^{13}CO, and $d = 140$ pc is the distance to HD 142527. For the $J = 2$–1 CO isotopologues, $B_e = 55.1$ GHz and $A_{21} = 3.04 \times 10^{-7} {\rm s}^{-1}$ for the line strength.[9] For the gas temperature we used $T = 43$ K, as calculated from ^{12}CO in the previous section.

We measured the integrated line intensity of ^{13}CO by summing the peak emission from the selected high velocity channels (see Section 3.1.2), under the approximation that the subtended solid angle is the same for all channels, and that the source is unresolved at these velocities, yielding $\hat{I} = 4.9 \times 10^{-10}$ W m^{-2}. This $\hat{I}$ gives a total column density of $N = (8.69 \pm 0.7) \times 10^{20}$ m^{-2}. This column corresponds to a total disk gas mass (H_2 plus CO) of $M_{\rm gas} = (1.7 \pm 0.6) \times 10^{-3}\, M_\odot$. Here, we have considered all the gas inside the dust-depleted cavity of 140 AU. The quoted thermal errors are 5σ (based on the noise levels in Table 1) and are subject to a further $\sim$10% flux calibration systematic uncertainty. The same procedure, if applied to the $C^{18}O$ emission, yields a gas mass of $M_{\rm gas} \sim 2 \times 10^{-3}\, M_\odot$.

Archival ALMA observations of $^{13}CO J = 3$–2 also show strong emission at channels with velocities $\langle +1.8\ {\rm km\ s^{-1}}$ and $\rangle + 5.4\ {\rm km\ s^{-1}}$, corroborating our detection of CO $J = 3$–2 gas inside the cavity (see Fukagawa et al. 2013, for a description of this data set). These observations show that $^{13}CO J = 3$–2 is mostly optically thick over the entire disk. The noise level on each of these channel map is 0.12 mJy beam^{-1} (Fukagawa et al. 2013). If we assume $C^{18}O J = 3$–2 is optically thin at least inside the cavity, the integrated line intensity amounts to $\hat{I} = 8.23 \times 10^{-10}$ W m^{-2}, which gives a total column of 1.1×10^{20} m^{-2} and a disk mass of $(1.1 \pm 0.6) \times 10^{-3}\, M_\odot$, consistent with the $J = 2$–1 estimate (5σ error bars). For this calculation we used the same procedure explained above to estimate the integrated line intensity arising from the cavity gas but with the corresponding constants, $B_e = 54.9$ GHz and $A_{32} = 2.17 \times 10^{-6} {\rm s}^{-1}$, for the $C^{18}O$ $J = 3$–2 molecule.

We conclude that there is still at least more than one Jupiter mass worth of gas inside the dust-depleted cavity. This gas is available to be accreted by possible forming planets and/or to be accreted onto the star. However, there are considerable uncertainties involved in this analysis, making this result only a crude estimate of the total gas mass. The main sources of uncertainty are the assumed isotopic line ratios and the gas temperature.

4. PHYSICAL STRUCTURE OF THE DISK

4.1. Parameterized Model

We adopted a simple, azimuthally symmetric parameterized structure for the disk gas density, where the vertical dimension is given by the hydrostatic equilibrium equation, such that

$$\rho(r, z) = \frac{\Sigma(r)}{\sqrt{2\pi}h} \exp\left[-\frac{1}{2}\left(\frac{z}{h}\right)^2\right], \quad (5)$$

[9] The spectral information for the CO molecule was obtained from the Splatalogue database.

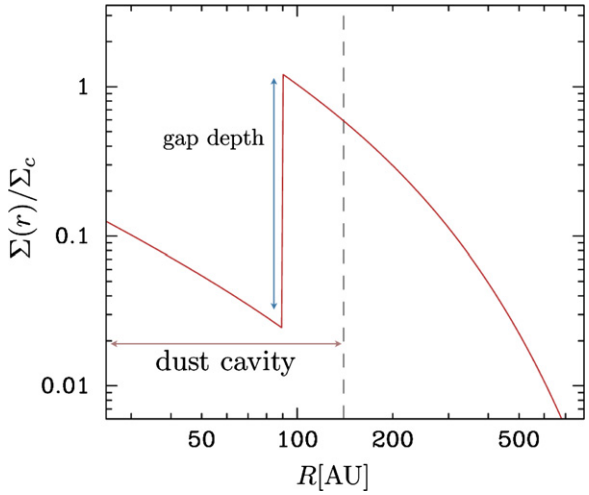

Figure 7. Model surface density profile (Equation (6)) of the disk.

where $h(r) = 0.1r$ is the disk scaleheight. The inner wall of the outer disk needs to subtends a large solid angle in order to explain the SED, as informed by Verhoeff et al. (2011). Equation (5) assumes the disk is isothermal in the vertical direction. The global surface density profile is a power law in radius with an exponential tapering at large radii, as described in Lynden-Bell & Pringle (1974; see also Andrews et al. 2011). The parametric equation reads

$$\Sigma(r) = \delta_{\rm gap} \Sigma_c \left(\frac{r}{R_c}\right)^{-\gamma} \exp\left[-\left(\frac{r}{R_c}\right)^{2-\gamma}\right], \quad (6)$$

where R_c is a characteristic radius and Σ_c is the surface density at that radius. The model disk structure is then separated into two distinct radial zones: a depleted inner cavity and an outer disk. The $\delta_{\rm gap}$ parameter is a scaling factor which accounts for the depletion inside the cavity ($r < R_{\rm cav}$). δ is a free parameter inside the cavity, and attains unity in the outer disk. See Figure 7 for a schematic representation of the surface density model. The inner zone of the disk is truncated at 0.3 AU, at which the temperature reaches $T = 1500$ K, sublimating dust particles.

The kinetic temperature of the gas is flat close to the star ($r < 50$ AU), with a warm temperature of 50 K. Farther out, we modeled the temperature with a power law, such that

$$T(r) = 50 \left(\frac{r}{50\ {\rm AU}}\right)^{-0.3} {\rm K}, \quad (7)$$

where the power-law slope and scaling factor were informed by the ^{12}CO optically thick emission (see Section 3.3.1). The disk is assumed to be vertically isothermal.

For simplicity, we assumed that the gas in the disk follows circular Keplerian rotation, such that

$$v_{\rm k}(r) = \sqrt{\frac{GM_\star}{r}}, \quad (8)$$

where $M_\star$ is the central mass star. Although hints of non-Keplerianity are seen in the ^{12}CO channel maps, these have a minor effect in our analysis. The velocity dispersion of the random motions of the gas (Doppler b-parameter) was fixed to 50 m s^{-1}.

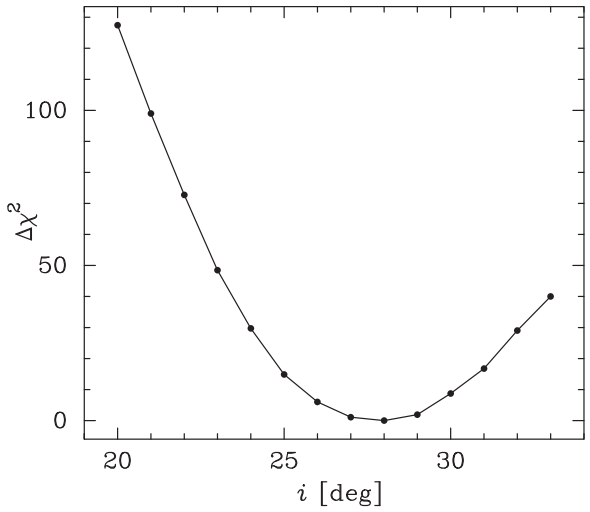

Figure 8. Plot of $\Delta\chi^2$ as a function of a single parameter, the inclination of the disk i. The curve has a minimum around $i = 28°$, with a 1σ error of $\pm 0.°5$.

The CO column density is given by

$$N_{\rm CO}(r) = \frac{X_{\rm CO}}{\mu m_{\rm H}} \Sigma(r), \quad (9)$$

where $X_{\rm CO}$ is the abundance of CO relative to H_2. We have assumed the ISM value.

Equations (5)–(9) fully describe the structure of the disk. The disk is then characterized by six parameters, Σ_c, R_c, γ, $R_{\rm cav}$, $M_\star$, and inclination i. The minor axis position angle is $\sim 70°$ as determined from the velocity maps. In order to compare with the Band 6 observations, the synthetic models of line emission were resampled and transformed to visibilities using the exact baseline information from the ALMA measurement set. We also calculate HD 142527's SED for our disk structure model. The results show consistency between our model and HD 142527's bulk properties (see the Appendix). It is important to note that these disk models have degeneracies. The models also assume an axisymmetric structure for the gas, but from HCO^+ observations we know there is a filamentary structure inside the cavity.

4.2. Modeling Results

We predicted the line radiation from the set of model disks using the three-dimensional nonlocal thermodynamic equilibrium (non-LTE) molecular excitation and radiative transfer code LIME (Brinch & Hogerheijde 2010). We generated channel maps matching the spectral resolution of the ALMA data cubes. Then, we extracted the uv-coverage information directly from the ALMA measurement sets to calculate model visibilities that match the exact Fourier sampling used in the observations. Our models were compared to the data in the visibility plane based on χ^2 statistics. The models were post-processed and CLEANed using the same strategy used to generate our ALMA maps. Finally, the best-fit models were contrasted with the data by visual inspection.

The model parameters that match the observations are listed in Table 2. A tapered disk slope of $\gamma = 1$ accounts for the extended size of the source in ^{12}CO. Inside the cavity, the $\delta_{\rm gap}$ parameter was set to 0.02, in order to reproduce our observed line fluxes. Higher values make the ^{13}CO appear optically thick inside the cavity. We estimate an uncertainty of 0.01 based on the optical thickness of the lines. It is worth mentioning that the slope of the density profile inside the cavity does not have to be necessarily decreasing with radius (see, for example, Tatulli et al. 2011, for HD 100546). A flat profile inside the cavity might also be valid, which would imply a shallower gap depth value. These possibilities will be further explored in a future paper.

Our method to estimate the inclination angle differs from previous approaches because it relies on the dynamics of the high velocity gas evidenced by the high velocity channels, whose spatial distribution strongly depends on inclination angle. Previous methods use scattered light and continuum images of the full disk. Continuum images trace the emitting material closer to the midplane hence giving an estimate of the inclination of the dust near the midplane. Our approach uses the dynamical model of the gas rotation, giving a good estimate of the gaseous disk's inclination.

There is a degeneracy between inclination angle, i, and the mass of the central star, $M_\star$, when trying to compute the kinematic signatures of the rotating gaseous disk. In order to break this degeneracy, we run a set of test models for a range

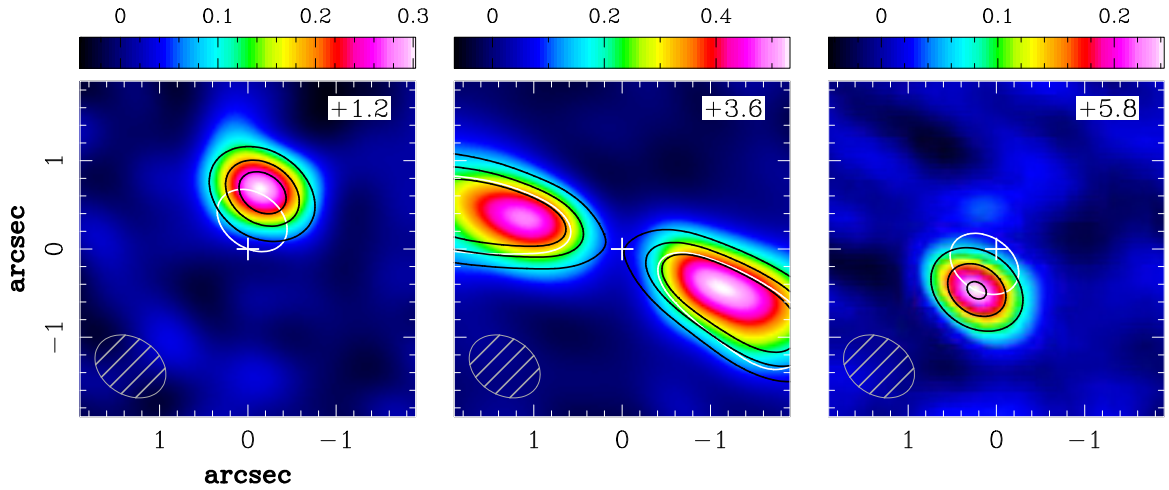

Figure 9. These panels show the best-fit model for the disk structure in HD 142527 in ^{13}CO emission. The model is presented in contours while the ALMA data are shown in false color. Black contours show the model with an inclination angle of 28° and a central star mass of 2.2 $M_\odot$, which best reproduces the observed morphology. The white contours show a similar model but with a disk inclination of 20 degrees only. Left: blue high velocity channel that shows gas coming from inside the cavity, close to the central. Center: systemic velocity channel. Right: red high velocity channel. See top wedge for contours and emission levels.

of values of $M_\star$ and i. The goodness of each fit was evaluated by calculating the reduced χ^2, which is defined as $\chi^2_\nu = \chi^2/\nu$, where ν is the number of the degrees of freedom. For these observations, the number of degrees of freedom is 10^7, which corresponds to the number of visibilities in each data set. The minimum χ^2_ν (best fit) is attained at $M_\star = 2.2\,M_\odot$ and it is equal to 1.001662. On the other hand, the values of $\Delta\chi^2_\nu$ (defined as $\chi^2_\nu - \min\{\chi^2_\nu\}$) for $M_\star$ equal to 2 and to 2.6 $M_\odot$ are 2×10^{-6} and 5×10^{-6}, respectively. Similar values were found for inclination angles ranging from 20° to 30°. According to our χ^2_ν fit in the visibility plane, the model with a central star mass $M_\star = 2.2\,M_\odot$ best reproduces our ^{13}CO data. After fixing the mass to this value, we estimate the disk's inclination angle.

Previous models for the disk in HD 142527 assumed a cavity size of 140 AU for both gas and dust and a disk inclination of 20° (Verhoeff et al. 2011; Casassus et al. 2013b). Although the overall multi-wavelength data are consistent with these parameters, they are unable to explain the observed spatio-kinematic morphologies of the CO emission lines. In order to reproduce the high velocity channel maps (wings of the lines), a significant increase in the projected velocity closer to the central star is needed. With a large disk inclination, $i = 28° \pm 0.°5$, we obtain a good match with the ALMA data, reproducing the ^{13}CO morphologies both at systemic velocity and in the high velocity wings. The excellent signal-to-noise in the high velocity channel maps allows us to determine the inclination of the disk with an accuracy of half a degree. Figure 8 shows a χ^2 plot for a distribution of inclination angles, calculated in the uv-plane.

After fixing the inclination angle at 28°, we varied the cavity radius in order to find a good match. The best fit for the cavity radius in the gas is 90±5 AU. The error was obtained from visual inspection of the plotted models against the ^{13}CO data. It is important to note that the inclination angle best characterizes the emission coming from inside the cavity. Our estimate of the inclination angle is consistent with the values determined by Fukagawa et al. (2013) from CO J = 3–2 observations.

Figure 9 shows our best-fit model for the structure of HD 142527 transition disk that accounts for the observed ^{13}CO emission. ^{13}CO is a tracer of the disk density distribution, it is optically thin inside the cavity and the maps have high signal-to-noise ratio. The best-fit model also matches the C^{18}O maps. The integrated density distribution of our disk model yields a total (dust plus gas) mass of the disk of 0.1 $M_\odot$, consistent with previous estimates based on millimeter continuum observations (Öberg et al. 2011).

5. DISCUSSION

We have conducted a detailed analysis of the ^{12}CO, ^{13}CO, and C^{18}O J = 2–1 line emission from HD 142527, focusing on the gas inside the dust-depleted cavity.

There are three main scenarios for clearing central cavities in disks; photoevaporation by high-energy photons, lowering of dust opacity due to grain-growth and dynamical clearing by a companion object. Casassus et al. (2013b) argued against photoevaporation in this source, based mainly on the high accretion rate and large size of the cavity. Our detection of large amounts of CO gas inside the cavity furthers the argument against photoevaporation as the main clearing mechanism. Moreover, there is evidence of the presence of a small inner disk inside the cavity (van Boekel et al. 2004; Verhoeff et al. 2011), which would hinder the efficiency of photoevaporating winds.

Dust continuum emission at 345 GHz has been detected with ALMA inside the cavity, but at very low levels and at the limit of the dynamic range. The exact morphology of this faint signal is sensitive on the details of image synthesis and self-calibration process. While Casassus et al. (2013b) find a filamentary morphology, matched to the gap-crossing filaments seen in HCO$^+$(4–3), Fukagawa et al. (2013) proposed a compact signal stemming from the inner disk only. Whichever the case, the peak signal at 345 GHz is an upper limit to the emission from millimeter-sized particles inside the cavity. The contrast between the bottom of the gap and the outer disk in surface density of millimeter-emitting grains is <300 (gap depth of about 0.003%).

Smaller dust particles, ~1 μm dust emitting in the near and mid-IR, have eluded detection inside the 90 AU gas cavity radius (Fukagawa et al. 2006; Casassus et al. 2012; Canovas et al. 2013), although the IR rings are contained in the submillimeter ring (see Supplementary information in Casassus et al. 2013b). This may imply that all the dust follows a general drop in density inside the 90 AU cavity. The polarimetric data provides upper limits on the surface brightness of the polarized intensity emitted from inside the cavity (Canovas et al. 2013).

The current paradigm in giant planet formation holds that planets are manifested indirectly by their imprinted marks on their progenitor disk. Wide gaps will be carved by massive or multiple forming planets (Dodson-Robinson & Salyk 2011; Zhu et al. 2011). The shape of the outer disk inner wall will depend on the planet mass, disk thickness and viscosity of the disk, and on the temperature structure in the disk wall itself (Crida et al. 2006). The torque of the outermost planet will affect strongly the shape of the inner wall. The tidal radius of a planet, the so-called Hill radius, is defined by

$$R_{\rm H} = a_p \left(\frac{M_p}{3M_\star}\right)^{1/3}, \qquad (10)$$

where a_p is the radius of the planet's orbit, M_p is the mass of the planet, and $M_\star$ is the mass of the central star. More massive companions have a large sphere of influence, suggesting that they could carve larger gaps with attenuated or tapered-off walls.

The cavity in HD 142527 has a smaller radius in gas than in dust milimeter continuum. In HCO$^+$(4–3) emission the cavity is even smaller, suggesting that the disk wall is not sharp or vertical but rather tapered off by a large gradient (see Figure 6). Multiple planets located closer to the star can explain the large size of the cavity (Dodson-Robinson & Salyk 2011; Zhu et al. 2011). A precise analysis of the gas and dust wall in HD 142527 from ALMA Band 6 and Band 7 data, based on hydrodynamical models, will be presented in a future publication.

6. SUMMARY

We detected and identified emission from inside the dust-depleted cavity in carbon monoxide isotopologue data of the gas-rich transition disk HD 142527, in the J = 2–1 line of ^{12}CO, ^{13}CO and C^{18}O. The ^{12}CO emission from the inner cavity is optically thick, while ^{13}CO and C^{18}O appear to be optically thin, providing probes of the temperature and density fields inside the cavity. The main results of our analysis can be summarized as follows.

1. We determined the gas mass inside the gap from the ^{13}CO and C^{18}O emission. We used two methods: direct measure-

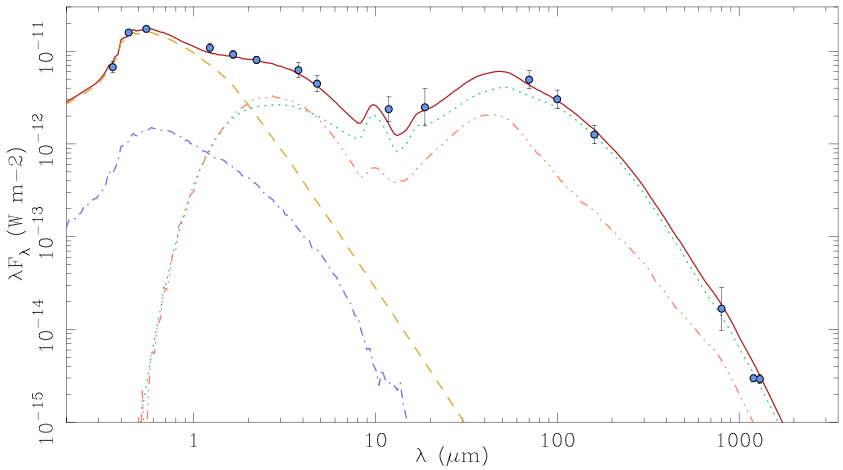

Figure 10. Dereddened photometry (blue dots) and spectral energy distribution model of HD 142527. Photometric data points have been obtained from Verhoeff et al. (2011). We have added the new ALMA continuum photometry at 1.2 mm. 5σ error bars are shown. The model contributions are: stellar spectrum alone (dashed yellow curve), scattered light from the star (dash-dotted light blue curve), thermal emission from inner and outer disks (dotted green curve), and scattered light from the dust thermal emission (dash triple dotted orange curve). The resulting model is the red solid curve.

ment of the optically thin lines and forward modeling using an axisymmetric disk. The total mass of gas surviving inside the cavity is high $(1.7 \pm 0.6) \times 10^{-3}\ M_{\odot}$.

2. We find that the inner cavity is rather small in CO gas, compared to its size in dust millimeter and infrared scattered light, with a best-fit radius of 90 ±5 AU.
3. The drop in density inside the cavity can be modeled as a reduction in gas column density of a factor of 50 (cavity depth of 0.02), given our model for the outer disk, which gives a total mass of 0.1 $M_{\odot}$.
4. The gap wall appears diffuse and tapered-off in the gas distribution, while in dust continuum is manifestly sharper.
5. The disk inclination is well constrained by the resolved velocity information of the CO gas and it attains 28 ± 0.5 degrees, after fixing the central star mass to 2.2 $M_{\odot}$.
6. The center of the disk appears shifted from a central continuum emission by a deprojected distance of ∼16 AU toward the East, assuming a distance of 140 pc to HD 142517.

We thank the anonymous referee for helpful comments and suggestions. S.P., G.v.d.P, S.C., and F.M. acknowledge support from the Millennium Science Initiative (Chilean Ministry of Economy), through grant "Nucleus P10-022-F." S.P., G.v.d.P., S.C., and P.R. acknowledge financial support provided by FONDECYT following grants 3140601, 3140393, 1130949, and 3140634. This paper makes use of the following ALMA data: ADS/JAO.ALMA#2011.0.00465.S. ALMA is a partnership of the ESO, NSF, NINS, NRC, NSC, and ASIAA. ALMA is a partnership of the ESO (representing its member states), NSF (USA), and NINS (Japan), together with the NRC (Canada) and NSC and ASIAA (Taiwan), in cooperation with the Republic of Chile. The National Radio Astronomy Observatory is a facility of the National Science Foundation operated under cooperative agreement by Associated Universities, Inc. P.R. acknowledges support from Project ALMA-CONICYT #31120006. C.P. acknowledges funding from the European Commission's 7th Framework Program (contract PERG06-GA-2009-256513) and from Agence Nationale pour la Recherche (ANR) of France under contract ANR-2010-JCJC-0504-01. L.C. acknowledges support from Project ALMA-CONICYT #31120009.

APPENDIX

SPECTRAL ENERGY DISTRIBUTION

We tested the consistency of our disk structure model by comparing its predicted SED against observed HD 142527 photometry. We obtained observed continuum fluxes from Verhoeff et al. (2011, see references therein). The observed SED was dereddened by using a standard extinction curve (Cardelli et al. 1989), for $A_V = 0.6$ (Verhoeff et al. 2011) and an assumed R_V of 3.1.

Synthetic fluxes were calculated using the Monte Carlo radiative transfer code MCFOST (Pinte et al. 2006). We used an MCFOST model consistent with the disk structure described in Section 4.1. Previous attempts to model the HD 142527 SED invoked a puffed-up rim to explain the large excess of emission in the near infrared (Verhoeff et al. 2011). This excess could be explained by the dust emission coming from very near the star that we see at 345 GHz (see Section 3.2).

We distributed dust grains (mainly silicates and amorphous carbons) with sizes between 0.1 and 1000 μm across the disk model. We used the Mie theory and assumed a gas-to-dust ratio of 100.

Figure 10 shows the SED calculated from our model. Our model consists of: (1) an inner disk extending from 0.2 to 6 AU with $10^{-9}\ M_{\odot}$ of dust. This dust mass, together with an aspect ratio h/r of 0.18, are enough to reproduce the large near-infrared excess; (2) a dust-depleted gap between 6 and 90 AU in radii almost depleted of gas and dust; (3) a second gap extending from 90 to 130 AU with enough gas to explain our isotopologues observations; and (4) a large outer disk stretching from 130 to 300 AU. The flaring exponent ranges between 1 and 1.18 for each zone. The aspect ratio of all the zones was 0.18 except for the outer disk which covers a larger solid angle, attaining an h/r of 0.23.

It is important to note that the gas model presented in Section 4.1 assumes a constant aspect ratio, since it only aims

to reproduce the gas inside the dust-depleted cavity and not the broad spectral features of the entire disk.

REFERENCES

Andrews, S. M., Wilner, D. J., Espaillat, C., et al. 2011, ApJ, 732, 42
Armitage, P. J. 2010, Astrophysics of Planet Formation (Cambridge: Cambridge Univ. Press), 294
Armitage, P. J. 2011, ARA&A, 49, 195
Avenhaus, H., Quanz, S. P., Schmid, H. M., et al. 2014, ApJ, 781, 87
Brinch, C., & Hogerheijde, M. R. 2010, A&A, 523, A25
Bruderer, S. 2013, A&A, 559, A46
Canovas, H., Ménard, F., Hales, A., et al. 2013, A&A, 556, A123
Casassus, S., Hales, A., de Gregorio, I., et al. 2013a, A&A, 553, A64
Casassus, S., Perez, M. S., Jordán, A., et al. 2012, ApJL, 754, L31
Casassus, S., Stahl, O., & Wilson, T. L. 2005, A&A, 441, 181
Casassus, S., van der Plas, G., M, S. P., et al. 2013b, Natur, 493, 191
Cardelli, J. A., Clayton, G. C., & Mathis, J. S. 1989, ApJ, 345, 245
Christiaens, V., Casassus, S., Perez, S., van der Plas, G., & Ménard, F. 2014, ApJL, 785, L12
Crida, A., Morbidelli, A., & Masset, F. 2006, Icar, 181, 587
Dodson-Robinson, S. E., & Salyk, C. 2011, ApJ, 738, 131
Fukagawa, M., Tamura, M., Itoh, Y., et al. 2006, ApJL, 636, L153
Fukagawa, M., Tsukagoshi, T., Momose, M., et al. 2013, PASJ, 65, L14
Högbom, J. A. 1974, A&AS, 15, 417
Horne, K., & Marsh, T. R. 1986, MNRAS, 218, 761
Lynden-Bell, D., & Pringle, J. E. 1974, MNRAS, 168, 603
Lyo, A.-R., Ohashi, N., Qi, C., Wilner, D. J., & Su, Y.-N. 2011, AJ, 142, 151
Malfait, K., Waelkens, C., Bouwman, J., de Koter, A., & Waters, L. B. F. M. 1999, A&A, 345, 181
McMullin, J. P., Waters, B., Schiebel, D., Young, W., & Golap, K. 2007, in ASP Conf. Ser. 376, Astronomical Data Analysis Software and Systems XVI, ed. R. A. Shaw, F. Hill, & D. J. Bell (San Francisco, CA: ASP), 127
Öberg, K. I., Qi, C., Fogel, J. K. J., et al. 2011, ApJ, 734, 98
Ohashi, N. 2008, Ap&SS, 313, 101
Pascucci, I., Sterzik, M., Alexander, R. D., et al. 2011, ApJ, 736, 13
Pinte, C., Ménard, F., Duchêne, G., & Bastien, P. 2006, A&A, 459, 797
Rameau, J., Chauvin, G., Lagrange, A.-M., et al. 2012, A&A, 546, A24
Rosenfeld, K. A., Chiang, E., & Andrews, S. M. 2014, ApJ, 782, 62
Stahl, O., Casassus, S., & Wilson, T. 2008, A&A, 477, 865
Tatulli, E., Benisty, M., Ménard, F., et al. 2011, A&A, 531, A1
van Boekel, R., Min, M., Leinert, C., et al. 2004, Natur, 432, 479
van Leeuwen, F. 2007, A&A, 474, 653
van der Plas, G., Casassus, S., Menard, F., et al. 2014, ApJ, 792, 25
Varnière, P., Blackman, E. G., Frank, A., & Quillen, A. C. 2006, ApJ, 640, 1110
Verhoeff, A. P., Min, M., Pantin, E., et al. 2011, A&A, 528, A91
Vilas-Boas, J. W. S., Myers, P. C., & Fuller, G. A. 2000, ApJ, 532, 1038
Wilson, T. L., Rohlfs, K., & Huumlttemeister, S. 2009, Tools of Radio Astronomy (Berlin: Springer)
Wilson, T. L., & Rood, R. 1994, ARA&A, 32, 191
Zhu, Z., Nelson, R. P., Hartmann, L., Espaillat, C., & Calvet, N. 2011, ApJ, 729, 47